ARTICLE IN PRESS

Communications Earth & Environment https://doi.org/10.1038/s43247-026-03253-0

Article in Press

Molecular fingerprinting of microbial consortia in late Oligocene microbialite architectures from a freshening Junggar paleolake, Central Asia

Received: 31 July 2025

Accepted: 22 January 2026

[redacted]

Cite this article as: Zhao, Z., Wu, C., Cui, X. *et al.* Molecular fingerprinting of microbial consortia in late Oligocene microbialite architectures from a freshening Junggar paleolake, Central Asia. *Commun Earth Environ* (2026). https://doi.org/10.1038/s43247-026-03253-0

Zhenle Zhao, Chaodong Wu, Xingqian Cui & Jian Ma

We are providing an unedited version of this manuscript to give early access to its findings. Before final publication, the manuscript will undergo further editing. Please note there may be errors present which affect the content, and all legal disclaimers apply.

If this paper is publishing under a Transparent Peer Review model then Peer Review reports will publish with the final article.

ARTICLE IN PRESS

© The Author(s) 2026. **Open Access** This article is licensed under a Creative Commons Attribution-NonCommercial-NoDerivatives 4.0 International License, which permits any non-commercial use, sharing, distribution and reproduction in any medium or format, as long as you give appropriate credit to the original author(s) and the source, provide a link to the Creative Commons licence, and indicate if you modified the licensed material. You do not have permission under this licence to share adapted material derived from this article or parts of it. The images or other third party material in this article are included in the article's Creative Commons licence, unless indicated otherwise in a credit line to the material. If material is not included in the article's Creative Commons licence and your intended use is not permitted by statutory regulation or exceeds the permitted use, you will need to obtain permission directly from the copyright holder. To view a copy of this licence, visit http://creativecommons.org/licenses/by-nc-nd/4.0/.

Molecular fingerprinting of microbial consortia in late Oligocene microbialite architectures from a freshening Junggar paleolake, Central Asia

Zhenle Zhao[1], Chaodong Wu[2], Xingqian Cui[1], Jian Ma[1*]

1. School of Oceanography, Shanghai Jiao Tong University, Shanghai, China
2. Key Laboratory of Orogenic Belts and Crustal Evolution, Ministry of Education, School of Earth and Space Sciences, Peking University, Beijing, China

Corresponding authors: J.M. (majian_geo@sjtu.edu.cn)

Abstract (<150 words)

Microbialites preserve crucial records of early life and geobiological processes, yet interpreting their formation mechanisms remains challenging. Here we analyze Oligocene oncolites from the Junggar Basin that retain exceptional lipid biomarkers due to limited diagenetic alteration. These spheroidal structures exhibit alternating calcite-rich laminae with Fe-Mn coatings, revealed through petrographic and elemental mapping. Lipid analysis identifies prokaryote-dominated communities, particularly phototrophs and heterotrophs, with carbonate-associated biomarkers indicating continuous microbial activity during growth. The release of saturated fatty acid derivatives through acid treatment further confirms exceptional organic preservation. We demonstrate that oncoid formation involved complex microbial consortia mediating calcification. These deposits correlate with accelerated Tianshan Mountain uplift, which triggered lake shallowing and turbulent conditions that enhanced benthic microbial productivity prior to Central Asian aridification. Our findings establish microbialites as sensitive indicators of coupled tectonic and environmental changes during the Oligocene-Miocene transition.

1 Introduction (~596 words)

Microbialites (e.g., stromatolites, thrombolites and related structures) form through interactions between microbial communities and their sedimentary environments[1, 2]. As some of oldest records of early life on the earth[3, 4, 5], microbialites preserve a continuous archive of geobiological evolution spanning billions of years[2], offering critical insights into origins of life[5, 6] and early environmental coevolution[7]. However, interpreting microbial metabolisms in ancient microbialites remains challenging due to the scarcity of unambiguous biosignatures, particularly in highly mineralized, fine-grained deposits[8].

Modern microbial mat sedimentation provides a valuable analogue for ancient microbialites, given their shared morphological and mineralogical[9, 10]. For example, laminated or columnar macrostructures occur consistently in both Precambrian and modern microbialites[11]. Similarly, carbonate nano-structures in microbialites, whether modern or ancient, may represent biosignatures resulting from bacterial calcification[12, 13, 14] or extracellular polymeric substance (EPS) mineralization[15, 16], while grain-trapping effects during microbial growth further reinforce these analogies[17, 18]. Despite advances in microbialite morphology and mineralogy, reliably attributing ancient microbialite formation to microbial activity, rather than abiotic precipitation, remains contentious without definitive fossilized microbial biogenicity[19, 20, 21].

Organic molecules offer critical insights into the role of microorganisms in microbialite formation[8, 22]. Lipid biomarkers, diagnostic organic compounds linked to specific organisms, have served as key tracers for reconstructing microbialite evolution and associated paleoenvironments throughout Earth history[23, 24, 25]. The prime example, hopanes, diagenetic derivatives of bacterial membrane hopanoids[26], are diagnostic for certain prokaryotes[27, 28, 29]. However, molecular interpretations in ancient rocks can be complicated by nonsyngenetic contaminants and thermal maturation[30, 31]. Conversely, lipid biomarkers can be preserved within inert sedimentary components. Sulfur-sequestered organic molecules, for instance, retain more indigenous signals than their free hydrocarbon counterparts[32, 33], while carbonate-associated lipids exhibit exceptional resistance to degradation, preserving otherwise labile biosignatures[34, 35]. Crucially, lipid incorporation into carbonate matrices likely occurs during microbial growth[36], suggesting this mechanism holds significant yet understudied potential for microbialite research. To date, however, related studies remain scarce.

Here, we report an Oligocene oncolitic succession from the Anjihaihe and Shawan Formations in the Manasi Section of the Junggar Basin, combining detailed biomarker analysis with optical and microscopic characterization. The Junggar Basin, currently bounded by the Altai, Zaire, and Tianshan Mountains in Central Asia (Fig. 1A, B), formed through multiple collision events and microplate amalgamation following Paleotethys closure during the Paleozoic[37, 38]. The southern Junggar Basin accumulated >10 km of sediments since the Late Permian[39] before experiencing Cenozoic uplift due to far-field effects of the India-Eurasia collision[40, 41]. The Tianshan Mountain experienced significant reactivation at ~24 Ma[42, 43, 44], exposing key outcrops including both our study site (Manasi Section) and the previously studied Anjihai Section ~50 km to the west[45] (Fig. 1 A). In both sections, the Oligocene-aged Anjihaihe Formation (32.7-23.3 Ma)[39, 46, 47] transitions conformably into the Shawan Formation. The Anjihaihe Formation records a deep lacustrine environment with gray-green mudstone-siltstone and calcite-dolomite interlayers showing evidence of photic zone euxinia[45] , shallowing upward into gray siltstone-sandstones and limestones. The overlying Shawan Formation features contrasting reddish sandstone-limestone deposits indicative of more oxidizing conditions.

Notably, the uppermost Anjihaihe Formation contains intermittent limestone layers hosting well-developed oncolite successions (Fig. 1C). As common microbialite constituents, oncolites form through combined rolling and biogenic encrustation processes, producing spheroidal structures with complex microbial architectures that often preserve exceptionally well[48]. These features have attracted considerable research interest for their formation mechanisms and environmental significance[49, 50, 51]. The Manasi Section oncolites exhibit clear internal microbialite structures (Fig. 2) and have experienced only moderate diagenetic alteration and thermal maturation, as established by our prior work in the Anjihai Section[45]. These characteristics make them ideal for investigating microbial consortia involved in microbialite formation.

2 Results and discussion (~2648 words)

2.1 Microbial architectures in Junggar oncolites through a multi-approach analysis

Large oncoids (8-12 cm in diameter) with well-developed spheroidal morphologies occur at the mudstone-limestone interface in the uppermost Anjihaihe Formation (Fig. 1). XRD analysis confirms their carbonate composition, with calcite dominating all samples (Supplementary Figure 1). This mineralogical signature is further supported by µXRF elemental mapping, which shows Ca as the predominant element with only minor Mg content (Fig. 2F).

Petrographic examination reveals that the Manasi Section oncolites consist primarily of concentric laminae exhibiting distinct morphological and color variations (Fig. 2A). These laminae display three characteristic microfabrics from core to cortex: (1) botryoidal structures in Zone A (nuclei), (2) irregular micritic fabrics in Zone B, and (3) isopachous layers in Zone C (Fig. 2B–D). Zone A comprises an assemblage of smaller oncoids and grains characterized by sparitic cores and well-developed micritic coatings. These structures exhibit distinct botryoidal textures within their laminations, which concentrically enclose the primary nucleus (Fig. 2D). Zone B contains heterogeneous micrite-microspar mixtures forming columnar, clotted, and smooth structures with highly variable layer thicknesses (µm to mm scale; Fig. 2E). µXRF analysis reveals two distinct elemental assemblages in Zone B: (1) Fe-Mn concentrations (likely from ferromanganese minerals) and (2) Al-K-Si enrichments (probably of siliciclastic origin; Supplementary Figure 2). In contrast to irregular fabrics in Zone B, Zone C exhibits isopachous micritic laminae of uniform micrometer-scale thickness, displaying alternating light and dark colored layers (Fig. 2B).

The laminae in Zones A and B of Junggar oncolites exhibit distinctive botryoidal and columnar microfabrics, respectively (Fig. 2D, C), morphological features commonly observed in both ancient stromatolites and modern microbial mats[52]. These structures find a potential modern analog in the oncoid deposits of Laguna Negra, Argentina[53], where botryoidal microfabrics form through the assemblage of smaller grains by biofilm decomposition and microbially induced precipitation. In this system, organic materials serve as nucleation sites for botryoidal crystals, which subsequently grow to encapsulate the organic matrix[54]. Comparable botryoidal aggregate formation has been documented in associations with cyanobacteria and diatoms[55, 56]. While diagenetic alteration typically prevents the preservation of biofilm remnants in ancient microbialites, the botryoidal microfabrics and homogeneous micritic calcite within Junggar oncolites suggest analogous biogeochemical processes. Specifically, the decomposition of microbial constituents likely facilitated localized Ca^{2+} release and enhanced carbonate nucleation efficiency[57, 58], mirroring the mechanisms observed in modern systems.

The columnar structures and fenestral porosity in Zone B (Fig. 2) of the Junggar oncolites resemble those observed in stromatolite biostromes and buildups, where hemispherical convex laminae progressively stack and accrete upon microbial mats[59]. This growth process is often accompanied by sediment trapping, where microbial communities capture and bind localized sediments passing across mat surfaces[60]. The development of microbial mats leads to the formation of fenestral structures, primarily through organic matter decay and mat desiccation[61]. These processes generate irregular surface topography that facilitate grain baffling[1]. In the Junggar oncolites, the co-enrichment of K, Al, and Si in Zone B (Fig. 2F) and their strong elemental correlations (Supplementary Figure 2A, B) reflect siliciclastic incorporation within oncoid structures. While microbial mats activity likely facilitated detrital trapping and binding, morphological and spatial distribution patterns also suggest significant later-stage pore-filling contributions. Notably, Fe and Mn show distinct enrichments in dark layers in Zone B and crusts in Zone A (Fig. 2F). The presence of ferromanganese oxides are tentatively identified by SEM-EDS analyses, including todorokite, recognized by its diagnostic reticulate morphology and Mn elemental signature[62] (Fig. 3A). While todorokite typically forms in marine Fe-Mn crusts and nodules under suboxic conditions[63, 64, 65], and can derive from birnessite through hydrothermal alteration[66], no hydrothermal evidence was detected in our samples. Instead, the nano-scale todorokite observed here aligns with biogenic occurrences documented in both modern and ancient microbialites[62] , likely formed through Mn-oxidizing bacterial activity[67] or bacterial biomediation[50, 68] given its distinctive nanostructure. Furthermore, micritic calcite in Zone B contains nanocrystalline iron oxide spheroids (Fig. 3C). Hematite was tentatively identified, as suggested by their nanoplate-spherical morphology[69] (Fig. 3D). Crucially, these nanostructures are associated with organic remnants (Fig. 3C and Supplementary Figure 1A, blue arrow), providing direct evidence for microbial involvement in ferromanganese oxide formation. The Fe-Mn enrichments are consistently associated with dark laminae, likely reflecting microbially-mediated oxidation processes, while Al-K-Si signals correlate with light laminae, indicating siliciclastic mineral incorporation. This distinct geochemical segregation is further corroborated by the presence of two distinct Fe-Si correlation trends (Supplementary Figure 2D), demonstrating the independent distribution patterns of ferromanganese oxides during oncoid growth. These observations collectively highlight the alternating influence of biogenic (Fe-Mn) and detrital (Al-K-Si) processes in lamina formation.

The isopachous laminae in Zone C of Junggar oncolites show striking similarities to those found in modern ooids and oolite deposits[52]. Ooids, spherical to ellipsoidal calcium carbonate concretions with concentric laminae of radially, tangentially, or randomly arranged crystals[70], remain enigmatic in their formation mechanisms. While the abiotic versus biotic origin of ooids continues to be debated[71, 72], microbial mediation through organomineralization likely contributes to their formation in many cases[36, 73]. In the Junggar oncolites, isopachous laminae in Zone C primarily consist of micrometer-scale amorphous micrites (Fig. 3B), which we interpret as amorphous calcium carbonate (ACC). This observation aligns with ACC precipitation documented in Bahamian ooids, where it has been proposed as a biomediated driver of ooid accretion[73]. The presence of organic remnants distributed within the ACC matrix of Zone C (Fig. 3B and Supplementary Figure 1B, blue arrow) suggests an analogous geobiological process operated in the Junggar system. However, potential contributions from abiotic chemically oscillating reactions[74] cannot be completely excluded.

2.2 Consortia complexity in forming microbial architectures

Beyond sedimentary evidence for microbial mediation in the Junggar oncolites, fossil lipid biomarkers, the geologically stable organic compounds derived from the diagenetic modification of biological precursors, are capable of fingerprinting organisms and, by extension, the geobiological process[23]. Hydrocarbon biomarkers extracted from Junggar oncolites revealed a diverse assemblage, including by long-chain *n*-alkanes (up to C_{33}) with significant odd-over-even predominance in the C_{23}–C_{31} range, indicative of terrestrial higher plant input[31],along with minor but diagnostic hopanoids (Supplementary Figure 3A). The co-occurrence of these biomarkers with well-preserved organic remnants observed in carbonate matrices (Supplementary Figure 4) suggest terrestrial organic matter was effectively incorporated and preserved through oncolite lamina formation.

The carbonate-associated hydrocarbon biomarkers display a comparable odd-over-even alkane preference but exhibit a distinct bimodal *n*-alkane distribution, with significantly greater abundance of short-chain alkanes (C_{15}–C_{19}) versus long-chain homologues (Supplementary Figure 3B). This pattern suggests preferential preservation of aquatic organic matter[31] within carbonate minerals during oncolite formation. Notably, hopanes show superior preservation relative to alkanes in the carbonate-bound fraction, indicating exceptional protection of microbial molecular signatures that may represent indigenous signals of microbial consortia involved in microbialite development. Intriguingly, the carbonate-associated hydrocarbons contain relatively higher concentrations of pyrene, a four-ring polycyclic aromatic hydrocarbon (PAH), compared to free hydrocarbon fractions (Supplementary Figure 3B). This selective enrichment implies strong adsorption of aromatic compounds during carbonate mineralization, consistent with known molecular preservation mechanisms governed by mineral-organic interactions[75]. However, the precise nature of PAH-carbonate associations requires further investigation to elucidate the underlying molecular-scale processes.

Significantly, we identified a suite of fatty acids (FAs) exclusively in the carbonate-associated lipid fraction (Fig. 4B, Supplementary Figure 5), which were absent from free lipids. This is a remarkable finding given that FAs are rarely preserved over geological timescales except in exceptional cases (e.g., Cretaceous-Paleocene rocks)[76, 77]. While modern systems show FAs as even-carbon-numbered chains during early organic decomposition[78], their diagenetic decarboxylation typically produces odd-numbered *n*-alkanes. The selective preservation of FAs in carbonate-associated fractions demonstrates their effective sequestration through carbonate mineralization[34, 79], in contrast to free FAs that likely underwent complete diagenetic conversion to alkanes. This unique mineral-lipid association provides critical insights into original microbial lipid signatures that would otherwise be lost to diagenetic alteration, offering a valuable window into ancient biogeochemical processes.

Carbon chain architecture (length, branching, and unsaturation) of fatty acids encodes essential information about their precursor organisms and biosynthetic pathways. Long-chain (>C_{20}) FAs typically derive from eukaryotes[80, 81], while shorter chains often reflect specific prokaryotic sources: cyanobacteria produce polyunsaturated C_{16} and C_{18} FAs (e.g., $FA_{16:0}$, $FA_{16:1}$, $FA_{18:2}$, $FA_{18:3}$ and $FA_{18:4}$)[82]. Gram-negative marine bacteria synthesize monounsaturated $C_{18:1}$[83], and Gram-positive bacteria yield abundant branched (anteiso/iso) FAs[84, 85]. In Junggar oncolites, carbonate-associated fractions exclusively contained saturated fatty acids dominated by $FA_{16:0}$ and $FA_{18:0}$, alongside longer chains up to $FA_{30:0}$ (Fig. 4B). We attribute this pattern to diagenetic saturation of originally polyunsaturated cyanobacterial fatty acids (particularly C_{16} and C_{18}), consistent with the Oligocene age of the samples. Supporting this interpretation, the odd-over-even predominance of C_{15}–C_{21} alkanes in carbonate phase matches the expected decarboxylation products of even-numbered FA_{16-22}. This molecular signature aligns with reported cyanobacterial biomarkers in stromatolites, including heptadecane/heptadecene and C_{17}–C_{22} alkenes[86]. The longer-chain fatty acids (C_{24}–C_{30}), characteristic of higher plant leaf waxes[81], likely originated from terrestrial higher plant debris incorporated during oncolite growth, as evidenced by siliciclastic laminae (Fig. 2).

Hopanes dominate the hydrocarbon biomarkers in Junggar oncolites, with steranes and carotenoids undetected by GC-MS. Although GC-QQQ-MS offers higher sensitivity for trace biomarkers, sterane concentrations remain remarkably low compared to hopanes (steranes/hopanes = 0.03, Supplementary Table 1), indicating prokaryote communities predominated over eukaryotes during oncolite formation. Notably, methylhopanes, particularly 2α-methyl-17α(H)-hopanes (2-MeH) and 3β-methyl-17α(H)-hopanes (3-MeH), show elevated concentrations, reaching 7.1% and 17.1% of C_{30} hopane, respectively. The 2-MeH derivatives originate from 2-methylbacteriohopanepolyols (2-MeBHPs), produced by diverse bacteria containing the *hpnP* gene[87]. While initially linked to aerobic/N_2-fixing cyanobacteria[27, 88], subsequent research has identified 2-MeBHP production in anoxygenic phototrophs (e.g., Rhodopseudomonas palustris)[89] and alphaproteobacteria[90]. Although not taxonomically exclusive, high 2-MeH abundances typically reflect environmental stress conditions[91, 92] particularly under anoxic/ferruginous[93] or low-oxygen/low-nitrogen regimes[90]. The 2-

methylhopane index (2-MHI)[27] in our samples (7.1%) significantly exceeds typical Phanerozoic values (<1%), approaching levels observed during extreme events like mass extinctions[94]. Combined with sedimentological and fatty acid evidence, this suggests cyanobacterial contributions under stressed conditions. The even higher 3-methylhopane index (3-MHI; 17.1-17.4%) points to Type I methanotrophic bacteria (γ-proteobacteria) containing the *hpnR* gene [95, 96, 97]. Unlike Type II methanotrophs, these thrive at low methane/oxygen concentrations near aerobic-anaerobic interfaces[98]. Although 3-MeBHPs have been recently identified in acidophilic phototrophs[99], their occurrence in the carbonate-rich Junggar environment appears unlikely. The exceptional preservation of fatty acids (FAs), coupled with the high abundance of 2-MeH and 3-MeH in carbonate phases, collectively indicates a diverse microbial consortium operating through redox fluctuations during oncolite formation. This biomarker pattern reflects alternating aerobic and anaerobic conditions that characterized the microbialite depositional environment.

The integration of organism-diagnostic lipid biomarkers and sedimentary evidence reveals a dynamic microbial consortium that drove organic-inorganic interactions during oncolite formation. Initially, carbonate nucleation was promoted in the Junggar lake with cyanobacteria accelerating precipitation through photosynthesis, as evidenced by petrographic patterns and biomarker assemblages. Although our lipid biomarker analysis utilized bulk oncolite samples, the preserved diagnostic molecules, when integrated with in situ petrographic observations, demonstrate that the characteristic light-dark banding formed through dynamic interplay between phototrophic oxygenic microbes and methanotrophic/heterotrophic communities. Specifically, oxygen produced by phototrophs served as a key oxidant for Fe (II) and Mn (II) fluxes derived from anoxic sediments, leading to the development of ferromanganese oxide crusts (Fig. 5, Stage A and B). The ubiquitous presence of iron oxide nanocrystal spheroids also provides clues for iron-oxidizing bacterial activity[100], which can catalyze Fe(II) oxidation and contributed to ferruginous crust formation. This redox coupling between microbial groups created self-reinforcing cycles of mineral precipitation and organic matter preservation within the developing oncolite laminae. Oxygen consumption established an aerobic-anaerobic transition zone, enabling Type I methanotrophs to thrive, while cyanobacteria utilized their CO_2 byproduct to further enhance carbonate production. This process led to preferential intracrystalline preservation of diagnostic microbial lipid biomarkers within carbonate phases. During oncoid laminae growth, siliciclastic minerals and terrestrial organic matter became incorporated through either intercrystalline infilling of microbial mat carbonates or physical trapping within surface topographies. Phototrophic-heterotrophic coupling and subsequent biomass decomposition generated substantial gas production, forming characteristic voids and fenestral structures (Fig. 2A). These gas pockets increased buoyancy[101], facilitating microbial mat flotation and tumbling to promote spheroidal morphogenesis. Hydrodynamic conditions critically modulated microfabric development: moderate flow regimes allowed microbial growth rates to exceed oncoid rotation, yielding irregular textures (Fig. 5, Stage B), whereas stronger currents induced rapid rotation that favored amorphous calcium carbonate precipitation and isopachous laminae formation via uniform mineral accretion (Fig. 5, Stage C). Collectively, these findings demonstrate how the unique microfabric zonation in Junggar oncolites emerged from synergistic interactions between redox-sensitive microbial metabolisms, mineral deposition processes, and physical hydrodynamics.

2.3 Evolving of microbial communities responding to Oligocene-Miocene environmental alternation

The enhanced aridification of Central Asia across Oligocene-Miocene represents one of the most significant Cenozoic climate changes in the northern hemisphere[102], driven by multiple factors including Tibetan Plateau uplift and westerlies[103, 104, 105], Paratethys Sea retreat[106, 107] and reorganization of atmospheric circulation under global cooling[108, 109]. Magnetostratigraphic dating of the southern Junggar Basin strata reveals a marked lithological transition from grayish-green to reddish sediments across the Oligocene-Miocene boundary (Anjihaihe to Shawan Formations)[39, 46, 47], coinciding with the onset of widespread aeolian deposition[102, 110] and desertification in the region (e.g., birth of Taklimakan Desert[111]). The oncolite layers capping the Anjihaihe Formation (dated to <23.3 Ma), developed immediately prior to this climatic shift, serving as a unique sedimentary archive of environmental conditions during this critical transition period. Their formation likely reflects lacustrine conditions that prevailed before the establishment of persistent arid regimes in Central Asia, as evidenced by the drastic environmental change recorded in strata across the southern Junggar Basin from west to east[45].

In-situ isotopic and elemental analyses of Junggar oncolites provide detailed insights into environmental changes during the Anjihaihe-Shawan Formation transition. The carbonate $\delta^{13}C$ and $\delta^{18}O$ records show distinct negative excursions (~5‰) in background calcite (Fig. 6A). Oncolite $\delta^{18}O$ values (-12.0‰ to -8.1‰) mirror this background trend, suggesting similar freshwater conditions during their growth. Zone B exhibits a ~3‰ $\delta^{18}O$ negative shift (Fig. 6D) coinciding with elevated Al/Ca and Si/Ca ratios (Fig. 6E), likely reflecting increased siliciclastic input from enhanced freshwater discharge. In contrast, oncolite $\delta^{13}C$ values show a pronounced ~6‰ positive excursion relative to background (Fig. 6A), potentially indicating the carbonate nucleation and accelerating precipitation through photosynthesis by cyanobacterial activity, as photosynthetic ^{12}C uptake enriches $\delta^{13}C$ in dissolved inorganic carbon (DIC) and promotes carbonate precipitation[112]. The minor $\delta^{13}C$ negative shift (1.1‰) in Zone B may reflect freshwater dilution effects or mediation by Fe-Mn oxidization bacteria. Notably, while Fe/Ca and Mn/Ca ratios remain stable throughout the oncolite layers (Fig. 6E), their peak concentrations at dark-light layer interfaces suggest microbially-mediated redox cycling. This pattern reflects periodic Fe-Mn oxide crust formation through oxygenic photosynthesis and subsequent metal oxidation at mat surfaces.

Our previous studies have established that the Anjihaihe Formation in the southern Junggar Basin experienced photic zone euxinia during its deep lake phase[45], as demonstrated by the presence of isorenieratane, a diagnostic biomarker for brown-colored green sulfur bacteria adapted to low-light conditions at depths ≤100 m[113, 114, 115]. A marked transition occurs in the upper Anjihaihe and overlying Shawan Formations, where sulfur bacterial biomarkers disappear while phototrophic and heterotrophic microbial communities flourish in oncolites, reflecting a rapid microbial community shift during lake shallowing and oxygenation preceding the Central Asian aridification. Distinct from the saline conditions of the Oligocene Anjihaihe Formation[116], negative $\delta^{13}C$ and $\delta^{18}O$ excursions in oncolites and background indicate freshwater input through regional drainage opening, likely driven by accelerated Tianshan Mountain uplift[47]. This tectonic event created west-east topographic gradients, turbulent hydrodynamic conditions, rapid lake shallowing, and enhanced benthic microbial proliferation, collectively promoting microbialite formation as a distinctive sedimentary response to these paleoenvironmental changes prior to regional drying. These findings are corroborated by similar conditions recorded in ~17 Ma stromatolites from the Taxihe Formation in the Taxihe Section (east of Manasi Section, Fig. 1A)[39], coinciding with the eastward migration of the Junggar Basin depocenter during Tianshan uplift[117], demonstrating the regional consistency of microbialite development during this transitional period[118]. Collectively, our results demonstrate that microbialites serve as high-resolution archives of coupled tectonic-environmental dynamics during the Oligocene-Miocene transition in Central Asia.

Materials and Methods

Petrology inspection and pretreatment. In total, six spherical oncolite samples, with 6–10 cm in diameter were collected from the oncolite successions in the upper Anjihaihe Fm. (Fig. 1, 6). Given the similar sedimentary patterns of all oncolite samples, one of the most representative oncolites, with an 8 cm maximum diameter (Fig. 2), was selected in this study. Overall, the spherical oncolite sample was spliced into 3 parts along the long axis, including two hemispheres (A, B) and a middle thin slab. The sawed slab was billeted and mounted for large-format thin section (9 x 10 cm) where petrographic observation and micro-X-ray fluorescence (μXRF) mapping were conducted. The hemisphere A was polished and prepared for microdrill sampling and scanning electron microscope (SEM), and the hemisphere B was grinded for X-Ray Diffraction (XRD) and biomarker analysis. Specifically, hemispheric sample B was sectioned using a diamond saw after removing the outer layers (~2 cm) to eliminate potential surface contamination. After sonicate-cleaning with the Milli-Q water and methanol for seconds (3 times by 10 s) and drying, the sawed and cleaned pieces were pulverized into fine powders using a zirconia grinding miller to ensure homogeneity. Before grinding each sample, combusted (550 °C, 12 h) clean sands were grinded in the same miller. Besides, all the equipment during the cracking and crushing was cleaned by Milli-Q water, dichloromethane (DCM) and methanol (MeOH) for 3 times, separately, to remove any potential mineral or organic contamination during grinding.

Micro-XRF mapping. The elemental mapping was conducted by a Bruker M4 Tornado table-top energy-dispersive µXRF scanner. Rhodium source was focused with polycapillary lens to achieve a smaller spot size (~25 µm) for a high-resolution elemental analysis. The excitation energy was set up at 30 W for a better-resolved point spectra and more accurate measurement. Most major elements (e.g., Ca, Mg, Fe, Mn, Al, S, K, Si…) were selected for mapping. The analytical repeatability and data stability were controlled by standard deviations of deconvolution in a Bruker ARTAX software[119] and the duplicated tests of the real sample (n=3). Results of µXRF elemental mapping presented as heat maps of multiple energy (Fig. 2F) and intensity curves (Fig. 6).

Microdrill sampling and C and O isotopic analysis. After cleaning with the Milli-Q water and drying, a microdriller, fixed with a 0.2 mm-drill bit, was adopted to obtain the layer-specific powders. Considering that the yellowish layers are largely mixed with white microspar layers, most grayish layers, spacing with ~3 mm, are selected (Fig. 6, red dots). During the microdrilling, areas with the development of microspar-clots were avoided. In total, powders from 10 different layers were collected (~500 mg each) for stable isotopes of carbonate phases. Briefly, stable C and O isotopes of drilled powders were determined using a Finnigan MAT 253 mass spectrometer linked to a ThermoFinnigan GasBench II. Devoid of organic matter, these calcite powders, was manually loaded into reacting containers with phosphoric acid, flushing with purified He gas. The reactant CO_2, after ~4 h reactions under 72 °C, was then released ten times into the mass spectrometer through a standard 100-µL sample loop. The $\delta^{18}O$ and $\delta^{13}C$ values are reported in per mil (‰) against the V-PDB (Vienna Pee Dee Belemnite) carbonate standard. The external precision was better than 0.1‰ for both $\delta^{13}C$ and $\delta^{18}O$.

SEM observation. After horizontally fixed on a glass plate, selected pieces with fresh surfaces from hemisphere A were mounted on a sputter-coated gold plate for the conduction of electric charges. The SEM observation was carried out using a FEI Quanta 650 FEG equipped with energy-dispersive spectrometry (EDS) detectors. Working voltage was set at 20 kV, and the microscale views were derived by modes of back scattered electrons (BSE) and secondary electrons (SE).

X-Ray Diffraction analysis. X-Ray Diffraction (XRD) analysis was conducted on the bulk powder for mineral identification. An aliquot of the bulk powder (~1 g) from the hemisphere B was pressed on a glass slide and scanned for 6 mins with a 2θ range of 5 ° to 80 ° on a D/max-rA rotating anode X-ray diffractometer (12 kW), manufactured by PANalytica. Mineral identification and semi-quantitative calculations were completed on the PANalytica program GSAS.

Organic extractions of free lipids. Another aliquot of the bulk powder (~6 g) from the hemisphere B was prepared for biomarker analysis. Total lipid extracts (TLE) were obtained by a sonication instrument with DCM/MeOH (9/1, v/v) at 60 °C for 30 mins in four times, and then concentrated under a steady stream of nitrogen gas. In contrast to the procedure blank, concentrated sample extracts displayed yellowish coloration.

Extraction of carbonate associated lipids. The extractable-lipids-free solid residue of the oncolite powders was subsequently transferred in a 250 mL beaker and then dissolved by hydrochloric acid (HCl, 2N). HCl drops were gradually added to control the viscous brown-colored foams during carbonate digestion. Eventually, concentrated HCl (6N) were replenished when no bubbles floated. After complete digestion overnight, the entire residue was diluted with Milli-Q water four times. As before, the carbonate-free residual was extracted for five times with DCM/MeOH (9/1, v/v) using the same sonicating protocol. The new extracts (denoted as carbonate associated lipids) were then concentrated under steady nitrogen stream and prepared for the fractionation.

Column chromatography fractionation and trimethylsilyl derivative treatment. After the removal of elemental sulfur by activated copper shots, two TLEs of oncolite, including free lipids and carbonate associated lipids, were separately loaded on in-house packed silica gel columns and then eluted into nonpolar and polar fractions with hexane/DCM (4:1, v/v) and DCM/MeOH (4:1, v/v) mixtures, sequentially. All the glassware was combustion at 550 °C for 12 h to remove any potential organic contamination. The non-polar fractions were proposed to gas chromatography (GC) analysis, and polar fractions were treated by trimethylsilyl derivatized by the reagent bis(trimethylsilyl)-trifluoroacetamide (BSTFA). In detail, polar fractions of free lipids and carbonate associated lipids were transferred in combusted (550 °C, 12 h) vials separately and dried. After adding 50 μL BSTFA and 50 μL anhydrous pyridine, the vails were capped tightly and heated at 70 °C for 1 h, and then subjected to GC analysis.

Lipid biomarker analysis. The measurements of n-alkanes, steranes and hopanes were conducted on gas chromatography mass spectrometry (GC-MS) and a gas chromatography triple quadrupole mass spectrometry (GC-QQQ-MS), sequentially. The GC-MS equips Agilent 6890A GC interfaced with an Agilent 5975C (MS), and the GC-QQQ-MS equips an Agilent 7890B GC system interfaced to an Agilent 7010 A triple quadrupole MS. All these GC instruments are installed with a DB-5MS column (60 m × 0.25 mm × 0.25 μm). During the lipid analysis, GC ovens were held isothermally at 40 °C for 1 min, then ramped to 320 °C, along with the maintained temperature at 250 °C and 300 °C for the source and transfer line, respectively. For the GC-MS, the MS source was set at 230 °C, the quadrupole was set to 150 °C, and the MS was operated in electron impact mode at 70eV. The scan range was set from 50 to 580 Da. The GC-QQQ-MS was operated in multiple reaction monitoring (MRM) mode, and the electron energy was set to 70 eV to ensure a standard signal for the precursor-product transitions. Biomarker data were analyzed on Agilent MassHunter software and each compound was identified in comparison with a composite oil standard provided by GeoMark Research Inc. The procedural blank was devoid of detectable levels of any organic compounds.

Data availability

All data generated from this study are included in the article and Supplementary Inventory.

Acknowledgements

Financial support at Shanghai Jiao Tong University (SJTU) is provided by the National Natural Science Foundation of China (42573024, 42203030, 42273075), the Shanghai Pujiang Programme (24PJA048) and the SJTU startup grant (WH220544005). Initial sampling, mineralogic and petrographic analysis were supported by the National Natural Science Foundation of China (42072125). J.M. gratefully acknowledges insightful discussions with Dr. Jingbo Chen at SJTU regarding mineral and XRD results, as well as technical support from Liqing Sun and Yan Zhu (Boyue Instruments, Shanghai) for μXRF analytical guidance. The authors sincerely appreciate the constructive comments provided by the editor and anonymous reviewers, which significantly improved the manuscript.

Author Contributions

J.M., and C.W. designed the research; Z.Z., X.C., and J.M. performed the biomarker analysis; Z.Z., and J.M. conducted mineral and isotopic analysis; Z.Z. and J.M. wrote the draft, and all authors have contributions on revising the manuscript.

Competing interests

The authors declare no competing interests.

Figure captions

Figure 1 The locations and stratigraphy of the Manasi and Anjihai Sections within the geological and geomorphological maps of the Junggar Basin of the Central Asia.

The geomorphological and geological maps illustrate the resent-day distribution of the Junggar Basin and surrounding mountains in the Central Asia (**B**), and overlapping Mesozoic–Cenozoic strata in the South Junggar Basin (**A**). The stratigraphic profiles are obtained from Manasi (this study) and Anjihai Sections[45] (**C-C, D**). Chronological constrains of two sections follow a previous magnetostratigraphy study[46] (**C-A, B**). Notably, in the middle–upper Anjihaihe Fm., photic zone euxinia (black circle) is developed as evidenced by high concentration of isorenieratane, a lipid biomarker that derived from low-light-adapted phototrophic green sulfur bacteria (GSB)[113]; while oncolite successions are developed at the interface of mudstone and limestone layers on the top of Anjihaihe Fm. The overlaying Shawan Fm. is featuring as oxidized-red coloration across the southern Junggar Basin. The satellite base map of the Central Asia is derived from Shuttle Radar Topography Mission (SRTM) database.

Figure 2 Petrographic images of the Junggar oncolite from a large-format thin section (9 x 10 cm) with micro-X-ray fluorescence elemental mapping in a selected area.

An integral petrographic scan of the Junggar oncolite (**A**) highlights the heterogeneity inside, which is characterized by botryoidal (**D**), irregular (**C**) and isopachous (**B**) microfabrics. Accordingly, three depositional Zones (Zone A – Zone C) are identified (**E**). The selected area, covering three Zones, is analyzed by micro-X-ray fluorescence as shown by heat maps of different elemental abundance (Mg, S, Fe, Mn, Ca, K, Al and Si) (**F**).

Figure 3 Scanning electron microscope (SEM) imaging in different depositional Zones of the Junggar oncolite, illustrating the micro- and nano-sized minerals of calcite and ferromanganese oxides verified by energy dispersive spectrometer (EDS) analysis.

Minerals in micritic laminae of the Junggar oncolite are featured by micro- and nano-sizes under SEM observation. Micrometer-scaled amorphous micrites (**B**) (denoted as amorphous calcium carbonate, ACC) are mostly distributed in isopachous laminae of the Zone C, while ferromanganese oxides are mostly developed in dark layers of the Zone B (**A, C** and **D**).

Specifically, todorokite (**A**) and nanocrystal spheroids of iron oxide (**C** and **D**) are identified based on the morphology and EDS analysis. Notably, organic remains are distributed among minerals (blue arrows). Higher magnification insets of SEM imaging are referred to Supplementary Figure 4.

Figure 4 Biomarker comparisons of free lipid (free extracts, free non-polar fractions) and carbonate-associated lipid fractions (carbonate bound lipids that obtained by acid treatment) of the Junggar oncolite. A. Multiple Reaction Monitoring (MRM) results of methylhopanes on GC-QQQ-MS. B. Total Ion Chromatogram (TIC) results of fatty acids after trimethylsilyl (TMS) derivatization on GC-MS.

In addition of C_{31} 17α,21β(H) homohopanes (αβS and αβR) and C_{31} 17β,21β(H) homohopanes (ββ), GC-QQQ-MS analysis (MRM mode, transition 426→205) reveals distinct methylhopane distributions in oncoid structures of the Anjihaihe Formation (**A**). The carbonate-associated lipids show exceptionally high 2-methylhopane (2-Me, 16.6%) and 3-methylhopane (3-Me, 17.4%) abundances compared to background levels of the Anjihaihe Fm. (0.9% and 1.6%, respectively)[45]. Notably, while free lipids contain substantial 3-Me (17.1%), their 2-Me content (7.1%) is less than half that of carbonate-bound counterparts. The detection of thermally sensitive ββ homohopanes confirms low thermal maturity throughout the section. Remarkably, saturated fatty acids (FAs, ranging from $FA_{12:0}$ to $FA_{30:0}$) exclusively preserved in carbonate-associated lipids following TMS derivatization (**B**), with free lipid extracts showing no detectable FAs on GC-MS (TIC).

Figure 5 The proposed grow model of mineral precipitation and associated microbial consortia in forming Junggar oncolites.

Figure 6 Outcrop photographs of oncolite successions in the Manasi Section and microscopic geochemical profiles of the selected area in the Junggar oncolite.

Oncolite successions are developed on the top of green-colored Anjihaihe Fm. (**C**), with the overlaying Shawan Fm. which is featuring as red coloration in the Manasi Section (**B**). $\delta^{13}C$ and $\delta^{18}O$ values of the selected layers show distinct excursions from the nuclei to the cortex (red dots, Supplementary Table 2) (**D**). Notably,$\delta^{13}C$ values of different oncolite layers are all positive comparing to the isotopic background[120] and the $\delta^{18}O$ values are similar to the background within an overall negative excursion trend (**A**). Elemental intensity curves, obtained by µXRF mapping (Al, Si, Fe and Mn, normalized to Ca), indicate enhanced siliciclastic components in the Zone B and intensified abundance of ferromanganese oxides in interlayers between dark and light laminae.

References

1. Riding R. Microbial carbonates: the geological record of calcified bacterial–algal mats and biofilms. *Sedimentology* **47**, 179–214 (2000).

2. Bosak T, Knoll AH, Petroff AP. The meaning of stromatolites. *Annual Review of Earth and Planetary Sciences* **41**, 21–44 (2013).

3. Lowe DR. Stromatolites 3,400-myr old from the Archean of Western Australia. *Nature* **284**, 441–443 (1980).

4. Walter M, Buick R, Dunlop J. Stromatolites 3,400–3,500 Myr old from the North pole area, Western Australia. *Nature* **284**, 443–445 (1980).

5. Wilmeth DT*, et al.* Evidence for benthic oxygen production in Neoarchean lacustrine stromatolites. *Geology* **50**, 907–911 (2022).

6. Nutman AP, Bennett VC, Friend CR, Van Kranendonk MJ, Chivas AR. Rapid emergence of life shown by discovery of 3,700-million-year-old microbial structures. *Nature* **537**, 535–538 (2016).

7. Lyons TW*, et al.* Co‐evolution of early Earth environments and microbial life. *Nature Reviews Microbiology* **22**, 572–586 (2024).

8. Benzerara K*, et al.* Nanoscale detection of organic signatures in carbonate microbialites. *Proceedings of the National Academy of Sciences* **103**, 9440–9445 (2006).

9. Laval B*, et al.* Modern freshwater microbialite analogues for ancient dendritic reef structures. *Nature* **407**, 626–629 (2000).

10. Wacey D, Gleeson D, Kilburn M. Microbialite taphonomy and biogenicity: new insights from NanoSIMS. *Geobiology* **8**, 403–416 (2010).

11. Grotzinger JP, Knoll AH. Stromatolites in Precambrian carbonates: evolutionary mileposts or environmental dipsticks? *Annual review of earth and planetary sciences* **27**, 313–358 (1999).

12. Sun F*, et al.* Methanogen microfossils and methanogenesis in Permian lake deposits. *Geology* **49**, 13–18 (2021).

13. Perri E, Tucker M. Bacterial fossils and microbial dolomite in Triassic stromatolites. *Geology* **35**, 207–210 (2007).

14. Sánchez-Román M*, et al.* Aerobic microbial dolomite at the nanometer scale: Implications for the geologic record. *Geology* **36**, 879–882 (2008).

15. Decho AW, Visscher PT, Reid RP. Production and cycling of natural microbial exopolymers (EPS) within a marine stromatolite. In: *Geobiology: objectives, concepts, perspectives*). Elsevier (2005).

16. Pentecost A. Association of cyanobacteria with tufa deposits: identity, enumeration, and nature of the sheath material revealed by histochemistry. *Geomicrobiology Journal* **4**, 285–298 (1985).

17. Reid RP*, et al.* The role of microbes in accretion, lamination and early lithification of modern marine stromatolites. *Nature* **406**, 989–992 (2000).

18. Gebelein CD. Distribution, morphology, and accretion rate of recent subtidal algal stromatolites, Bermuda. *J Sediment Res* **39**, 49–69 (1969).

19. Grotzinger JP, Rothman DH. An abiotic model for stromatolite morphogenesis. *Nature* **383**, 423–425 (1996).

20. Allwood AC, Rosing MT, Flannery DT, Hurowitz JA, Heirwegh CM. Reassessing evidence of life in 3,700-million-year-old rocks of Greenland. *Nature* **563**, 241–244 (2018).

21. Lowe DR. Abiological origin of described stromatolites older than 3.2 Ga. *Geology* **22**, 387–390 (1994).

22. Zuckerkandl E, Pauling L. Molecules as documents of evolutionary history. *Journal of theoretical biology* **8**, 357–366 (1965).

23. Summons RE, Welander PV, Gold DA. Lipid biomarkers: molecular tools for illuminating the history of microbial life. *Nature Reviews Microbiology* **20**, 174–185 (2022).

24. Naeher S, Cui X, Summons RE. Biomarkers: molecular tools to study life, environment, and climate. *Elements: An International Magazine of Mineralogy, Geochemistry, and Petrology* **18**, 79–85 (2022).

25. Briggs DE, Summons RE. Ancient biomolecules: their origins, fossilization, and role in revealing the history of life. *BioEssays* **36**, 482–490 (2014).

26. Ourisson G, Albrecht P, Rohmer M. The hopanoids: palaeochemistry and biochemistry of a group of natural products. *Pure and Applied Chemistry* **51**, 709–729 (1979).

27. Summons RE, Jahnke LL, Hope JM, Logan GA. 2-Methylhopanoids as biomarkers for cyanobacterial oxygenic photosynthesis. *Nature* **400**, 554–557 (1999).

28. Summons RE, Jahnke LL. Identification of the methylhopanes in sediments and petroleum. *Geochim Cosmochim Acta* **54**, 247–251 (1990).

29. Farrimond P, Talbot H, Watson D, Schulz L, Wilhelms A. Methylhopanoids: molecular indicators of ancient bacteria and a petroleum correlation tool. *Geochim Cosmochim Acta* **68**, 3873–3882 (2004).

30. French K, Rocher D, Zumberge J, Summons R. Assessing the distribution of sedimentary C 40 carotenoids through time. *Geobiology* **13**, 139–151 (2015).

31. Peters KE, Walters CC, Moldowan JM. *The Biomarker Guide*. Cambridge University Press (2005).

32. Ma J, French KL, Cui X, Bryant DA, Summons RE. Carotenoid biomarkers in Namibian shelf sediments: Anoxygenic photosynthesis during sulfide eruptions in the Benguela Upwelling System. *Proceedings of the National Academy of Sciences* **118**, (2021).

33. Ma J, Cui X, Liu X-l, Wakeham SG, Summons RE. Rapid sulfurization obscures carotenoid distributions in modern euxinic environments. *Geochim Cosmochim Acta*, (2024).

34. Yang H, Ma J, He S, Wang J, Sun Y, Cui X. Resistant degradation of petrogenic organic carbon in the weathering of calcareous rocks. *Global and Planetary Change*, 104727 (2025).

35. Grice K, Holman AI, Plet C, Tripp M. Fossilised biomolecules and biomarkers in carbonate concretions from Konservat-Lagerstätten. *Minerals* **9**, 158 (2019).

36. Summons R, Bird L, Gillespie A, Pruss S, Roberts M, Sessions A. Lipid biomarkers in ooids from different locations and ages: evidence for a common bacterial flora. *Geobiology* **11**, 420–436 (2013).

37. Charvet J*, et al.* Palaeozoic tectonic evolution of the Tianshan belt, NW China. *Science China Earth Sciences* **54**, 166–184 (2011).

38. Wang J*, et al.* Source-to-sink analysis of a transtensional rift basin from syn-rift to uplift stages. *J Sediment Res* **89**, 335–352 (2019).

39. Ji J, Zhu M, Wang X, Luo P, Dong X. Ages of the Cenozoic strata on the southern margin of Junggar Basin, Northwestern China. *J Stratigr* **34**, 43–50 (2010).

40. Xiao W, Windley BF, Allen MB, Han C. Paleozoic multiple accretionary and collisional tectonics of the Chinese Tianshan orogenic collage. *Gondwana Research* **23**, 1316–1341 (2013).

41. Yang W, Jolivet M, Dupont‐Nivet G, Guo Z, Zhang Z, Wu C. Source to sink relations between the Tian Shan and Junggar Basin (northwest China) from Late Palaeozoic to Quaternary: evidence from detrital U‐Pb zircon geochronology. *Basin Research* **25**, 219–240 (2013).

42. Avouac J-P, Tapponnier P, Bai M, You H, Wang G. Active thrusting and folding along the northern Tien Shan and late Cenozoic rotation of the Tarim relative to Dzungaria and Kazakhstan. *Journal of Geophysical Research: Solid Earth* **98**, 6755–6804 (1993).

43. Yin A*, et al.* Late Cenozoic tectonic evolution of the southern Chinese Tian Shan. *Tectonics* **17**, 1–27 (1998).

44. Guo Z, Zhang Z, Wu c, Fang S, Zhang R. The Mesozoic and Cenozoic exhumation history of Tianshan and comparative studies to the Junggar and Altai Mountains. *Acta Geologica Sinica* **80**, 1–15 (2006).

45. Ma J*, et al.* Discovery of carotenoids and its paleolake significance in the Oligocene Anjihaihe Formation, southern Junggar Basin, China. *ACTA GEOLOGICA SINICA* **94**, 1853–1868 (2020).

46. Ji J, Luo P, White P, Jiang H, Gao L, Ding Z. Episodic uplift of the Tianshan Mountains since the late Oligocene constrained by magnetostratigraphy of the Jingou River section, in the southern margin of the Junggar Basin, China. *Journal of Geophysical Research* **113**, (2008).

47. Charreau J*, et al.* Neogene uplift of the Tian Shan Mountains observed in the magnetic record of the Jingou River section (northwest China). *Tectonics* **28**, n/a–n/a (2009).

48. Peryt TM. Classification of coated grains. In: *Coated grains*). Springer (1983).

49. Védrine S, Strasser A, Hug W. Oncoid growth and distribution controlled by sea-level fluctuations and climate (Late Oxfordian, Swiss Jura Mountains). *Facies* **53**, 535–552 (2007).

50. Schaefer MO, Gutzmer J, Beukes NJ. Late Paleoproterozoic Mn-rich oncoids: Earliest evidence for microbially mediated Mn precipitation. *Geology* **29**, 835–838 (2001).

51. Dahanayake K, Gerdes G, Krumbein WE. Stromatolites, oncolites and oolites biogenically formed in situ. *Naturwissenschaften* **72**, 513–518 (1985).

52. Flügel E, Munnecke A. *Microfacies of carbonate rocks: analysis, interpretation and application*. Springer (2010).

53. Buongiorno J, Gomez FJ, Fike DA, Kah LC. Mineralized microbialites as archives of environmental evolution, Laguna Negra, Catamarca Province, Argentina. *Geobiology* **17**,

199–222 (2019).

54. Gomez FJ, Kah LC, Bartley JK, Astini RA. Microbialites in a high-altitude andean lake: multiple controls on carbonate precipitation and lamina accertion in high-altitude lacustrine microbialites. *Palaios* **29**, 233–249 (2014).

55. Arp G*, et al.* Photosynthesis versus exopolymer degradation in the formation of microbialites on the atoll of Kiritimati, Republic of Kiribati, Central Pacific. *Geomicrobiology Journal* **29**, 29–65 (2012).

56. Winsborough BM, Golubić S. The role of diatoms in stromatolite growth: two examples from modern freshwater settings 1. *Journal of Phycology* **23**, 195–201 (1987).

57. Decho AW. Overview of biopolymer-induced mineralization: what goes on in biofilms? *Ecological Engineering* **36**, 137–144 (2010).

58. Visscher PT, Stolz JF. Microbial mats as bioreactors: populations, processes, and products. In: *Geobiology: objectives, concepts, perspectives*). Elsevier (2005).

59. Riding RE. *Microbial sediments*. Springer Science & Business Media (2000).

60. Black M. The algal sediments of Andros Island, Bahamas. *Philosophical Transactions of the Royal Society of London Series B, Containing Papers of a Biological Character* **222**, 165–192 (1932).

61. Pamela Reid R, James NP, Macintyre IG, Dupraz CP, Burne RV. Shark Bay stromatolites: microfabrics and reinterpretation of origins. *Facies* **49**, 299–324 (2003).

62. Ren Y*, et al.* Nano-mineralogy and growth environment of Fe-Mn polymetallic crusts and nodules from the South China Sea. *Frontiers in Marine Science* **10**, 1141926 (2023).

63. Usui A, Mellin TA, Nohara M, Yuasa M. Structural stability of marine 10 Å manganates from the Ogasawara (Bonin) Arc: Implication for low-temperature hydrothermal activity. *Marine geology* **86**, 41–56 (1989).

64. Bodeï S, Manceau A, Geoffroy N, Baronnet A, Buatier M. Formation of todorokite from vernadite in Ni-rich hemipelagic sediments. *Geochim Cosmochim Acta* **71**, 5698–5716 (2007).

65. Conrad T, Hein JR, Paytan A, Clague DA. Formation of Fe-Mn crusts within a continental margin environment. *Ore Geology Reviews* **87**, 25–40 (2017).

66. Atkins AL, Shaw S, Peacock CL. Nucleation and growth of todorokite from birnessite: Implications for trace-metal cycling in marine sediments. *Geochim Cosmochim Acta* **144**, 109–125 (2014).

67. Akai J, Iida A, Akai K, Chiba A. Mn and Fe minerals of possible biogenic origin from two Precambrian stromatolites in western Australia. *The Geological Society of Japan* **103**, 484–488 (1997).

68. Giresse P, Wiewiora A, Lacka B. Processes of Holocene ferromanganese-coated grains (oncolites) in the nearshore shelf of Cameroon. *J Sediment Res* **68**, (1998).

69. Tan W, Liang Y, Xu Y, Wang M. Structural-controlled formation of nano-particle hematite and their removal performance for heavy metal ions: A review. *Chemosphere* **306**, 135540 (2022).

70. Wright V, Tucker M. Carbonate sediments and limestones: constituents. *Carbonate Sedimentology Blackwell, Oxford*, 1–27 (1990).

71. Duguid SM, Kyser TK, James NP, Rankey EC. Microbes and ooids. *J Sediment Res* **80**, 236–251 (2010).

72. Diaz MR*, et al.* Geochemical evidence of microbial activity within ooids. *Sedimentology* **62**, 2090–2112 (2015).

73. Diaz MR, Eberli GP, Blackwelder P, Phillips B, Swart PK. Microbially mediated organomineralization in the formation of ooids. *Geology* **45**, 771–774 (2017).

74. Papineau D, Yin J, Devine KG, Liu D, She Z. Chemically oscillating reactions during the diagenetic formation of Ediacaran siliceous and carbonate botryoids. *Minerals* **11**, 1060 (2021).

75. Ingalls AE, Aller RC, Lee C, Wakeham SG. Organic matter diagenesis in shallow water carbonate sediments. *Geochim Cosmochim Acta* **68**, 4363–4379 (2004).

76. Abelson PH, Hoering TC, Parker PL. Fatty acids in sedimentary rocks. *Advances in Organic Geochemistry*, 169–174 (2013).

77. Kvenvolden KA. Molecular distributions of normal fatty acids and paraffins in some Lower Cretaceous sediments. *Nature* **209**, 573–577 (1966).

78. Gaines SM, Eglinton G, Rullkotter J. *Echoes of life: what fossil molecules reveal about earth history*. Oxford University Press (2008).

79. Qafoku O*, et al.* Chemical composition, coordination, and stability of Ca–organic associations in the presence of dissolving calcite. *Environmental Science: Nano* **10**, 1504–1517 (2023).

80. Harwood JL, Russell NJ, Harwood JL, Russell NJ. Major lipid types in plants and micro-organisms. *Lipids in plants and microbes*, 7–34 (1984).

81. Eglinton G, Hamilton RJ. Leaf Epicuticular Waxes: The waxy outer surfaces of most plants display a wide diversity of fine structure and chemical constituents. *science* **156**, 1322–1335 (1967).

82. Kenyon C. Fatty acid composition of unicellular strains of blue-green algae. *Journal of bacteriology* **109**, 827–834 (1972).

83. Oliver JD, Colwell RR. Extractable lipids of gram-negative marine bacteria: phospholipid composition. *Journal of bacteriology* **114**, 897–908 (1973).

84. Navarrete A*, et al.* Physiological status and community composition of microbial mats of the Ebro Delta, Spain, by signature lipid biomarkers. *Microbial Ecology* **39**, 92–99 (2000).

85. Ibekwe AM, Kennedy AC. Phospholipid fatty acid profiles and carbon utilization patterns for analysis of microbial community structure under field and greenhouse conditions. *FEMS microbiology ecology* **26**, 151–163 (1998).

86. Allen MA, Neilan BA, Burns BP, Jahnke LL, Summons RE. Lipid biomarkers in Hamelin Pool microbial mats and stromatolites. *Organic Geochemistry* **41**, 1207–1218 (2010).

87. Welander PV, Coleman ML, Sessions AL, Summons RE, Newman DK. Identification of a methylase required for 2-methylhopanoid production and implications for the interpretation of sedimentary hopanes. *Proceedings of the National Academy of Sciences* **107**, 8537–8542 (2010).

88. Kuypers MM, van Breugel Y, Schouten S, Erba E, Damsté JSS. N2-fixing cyanobacteria supplied nutrient N for Cretaceous oceanic anoxic events. *Geology* **32**, 853–856 (2004).

89. Rashby SE, Sessions AL, Summons RE, Newman DK. Biosynthesis of 2-methylbacteriohopanepolyols by an anoxygenic phototroph. *Proceedings of the National Academy of Sciences* **104**, 15099–15104 (2007).

90. Ricci JN*, et al.* Diverse capacity for 2-methylhopanoid production correlates with a specific ecological niche. *The ISME journal* **8**, 675–684 (2014).

91. Garby TJ*, et al.* Lack of methylated hopanoids renders the cyanobacterium Nostoc punctiforme sensitive to osmotic and pH stress. *Applied and Environmental Microbiology* **83**, e00777–00717 (2017).

92. Wu C-H, Bialecka-Fornal M, Newman DK. Methylation at the C-2 position of hopanoids increases rigidity in native bacterial membranes. *Elife* **4**, e05663 (2015).

93. Eickhoff M, Birgel D, Talbot H, Peckmann J, Kappler A. Oxidation of F e (II) leads to increased C ‐ 2 methylation of pentacyclic triterpenoids in the anoxygenic phototrophic bacterium R hodopseudomonas palustris strain TIE ‐ 1. *Geobiology* **11**, 268–278 (2013).

94. Naafs B, Bianchini G, Monteiro FM, Sánchez‐Baracaldo P. The occurrence of 2‐methylhopanoids in modern bacteria and the geological record. *Geobiology* **20**, 41–59 (2022).

95. Rohmer M, Bouvier-Nave P, Ourisson G. Distribution of hopanoid triterpenes in prokaryotes. *Microbiology* **130**, 1137–1150 (1984).

96. Zundel M, Rohmer M. Prokaryotic triterpenoids: 1. 3β‐Methylhopanoids from Acetobacter species and Methylococcus capsulatus. *European Journal of Biochemistry* **150**, 23–27 (1985).

97. Welander PV, Summons RE. Discovery, taxonomic distribution, and phenotypic characterization of a gene required for 3-methylhopanoid production. *Proceedings of the National Academy of Sciences* **109**, 12905–12910 (2012).

98. Hanson RS, Hanson TE. Methanotrophic bacteria. *Microbiological reviews* **60**, 439–471 (1996).

99. Mayer MH, Parenteau MN, Kempher ML, Madigan MT, Jahnke LL, Welander PV. Anaerobic 3-methylhopanoid production by an acidophilic photosynthetic purple bacterium. *Archives of Microbiology* **203**, 6041–6052 (2021).

100. Emerson D, Fleming EJ, McBeth JM. Iron-oxidizing bacteria: an environmental and genomic perspective. *Annual review of microbiology* **64**, 561–583 (2010).

101. Zhao C, Shi M, Lei Y, Feng Q. Silicified floating microbial mats from the Mesoproterozoic Wumishan Formation, North China: preservation and ecological significance. *Precambrian Research* **425**, 107816 (2025).

102. Guo Z*, et al.* Onset of Asian desertification by 22 Myr ago inferred from loess deposits in China. *Nature* **416**, 159–163 (2002).

103. Manabe S, Broccoli A. Mountains and arid climates of middle latitudes. *Science* **247**, 192–195 (1990).

104. An Z, Kutzbach JE, Prell WL, Porter SC. Evolution of Asian monsoons and phased uplift of the Himalaya–Tibetan plateau since Late Miocene times. *nature* **411**, 62–66 (2001).

105. Wang X*, et al.* The role of the westerlies and orography in Asian hydroclimate since the late Oligocene. *Geology* **48**, 728–732 (2020).

106. Ramstein G, Fluteau F, Besse J, Joussaume S. Effect of orogeny, plate motion and land–sea distribution on Eurasian climate change over the past 30 million years. *Nature* **386**, 788–795 (1997).

107. Miao Y, Herrmann M, Wu F, Yan X, Yang S. What controlled Mid–Late Miocene long-

term aridification in Central Asia?—Global cooling or Tibetan Plateau uplift: A review. *Earth-Science Reviews* **112**, 155–172 (2012).

108. Licht A*, et al.* Asian monsoons in a late Eocene greenhouse world. *Nature* **513**, 501–506 (2014).

109. Bosboom RE, Abels HA, Hoorn C, van den Berg BC, Guo Z, Dupont-Nivet G. Aridification in continental Asia after the middle Eocene climatic optimum (MECO). *Earth Planet Sci Lett* **389**, 34–42 (2014).

110. Sun J*, et al.* Late Oligocene–Miocene mid-latitude aridification and wind patterns in the Asian interior. *Geology* **38**, 515–518 (2010).

111. Zheng H*, et al.* Late oligocene–early miocene birth of the Taklimakan Desert. *Proceedings of the National Academy of Sciences* **112**, 7662–7667 (2015).

112. Song BW, Ji JL, Wang CW, Xu YD, Zhang KX. Intensified aridity in the Qaidam Basin during the Middle Miocene: constraints from ostracod, stable isotope, and weathering records. *Can J Earth Sci* **54**, 242–256 (2017).

113. Overmann J, Cypionka H, Pfennig N. An extremely low - light adapted phototrophic sulfur bacterium from the Black Sea. *Limnology and Oceanography* **37**, 150–155 (1992).

114. Repeta D, Simpson D, Jorgensen B, Jannasch H. Evidence for anoxygenic photosynthesis from the distribution of bacterio-chlorophylls in the Black Sea. *Nature* **342**, 69–72 (1989).

115. Sylvan JB, Toner BM, Edwards KJ. Life and death of deep-sea vents: bacterial diversity and ecosystem succession on inactive hydrothermal sulfides. *MBio* **3**, e00279–00211 (2012).

116. Li Q, Li L, Zhang Y, Guo Z. Oligocene incursion of the Paratethys seawater to the Junggar Basin, NW China: insight from multiple isotopic analysis of carbonate. *Scientific Reports* **10**, 6601 (2020).

117. Zhou Y*, et al.* Cenozoic tectonic patterns and their controls on growth strata in the northern Tianshan fold and thrust belt, northwest China. *Journal of Asian Earth Sciences* **198**, 104237 (2020).

118. Yang W*, et al.* Sensitivity of lacustrine stromatolites to Cenozoic tectonic and climatic forcing in the southern Junggar Basin, NW China: New insights from mineralogical, stable and clumped isotope compositions. *Palaeogeography, Palaeoclimatology, Palaeoecology* **514**, 109–123 (2019).

119. Rousseau RM. Detection limit and estimate of uncertainty of analytical XRF results. *Rigaku J* **18**, 33–47 (2001).

120. Li Q, Zhang Y, Dong L, Guo Z. Oligocene syndepositional lacustrine dolomite: A study from the southern Junggar Basin, NW China. *Palaeogeography, Palaeoclimatology, Palaeoecology* **503**, 69–80 (2018).

Editorial summary:

Oligocene-aged microbialites preserved intact lipid biomarkers, revealing microbial activity and oncolite growth. Advanced geochemical and imaging techniques decoded these microbial "time capsules" at unprecedented resolution.

Peer review information:

Communications Earth and Environment thanks Agustina I. Lencina and the other, anonymous, reviewer(s) for their contribution to the peer review of this work. Primary Handling Editors: Deborah Tangunan and Alireza Bahadori. A peer review file is available.

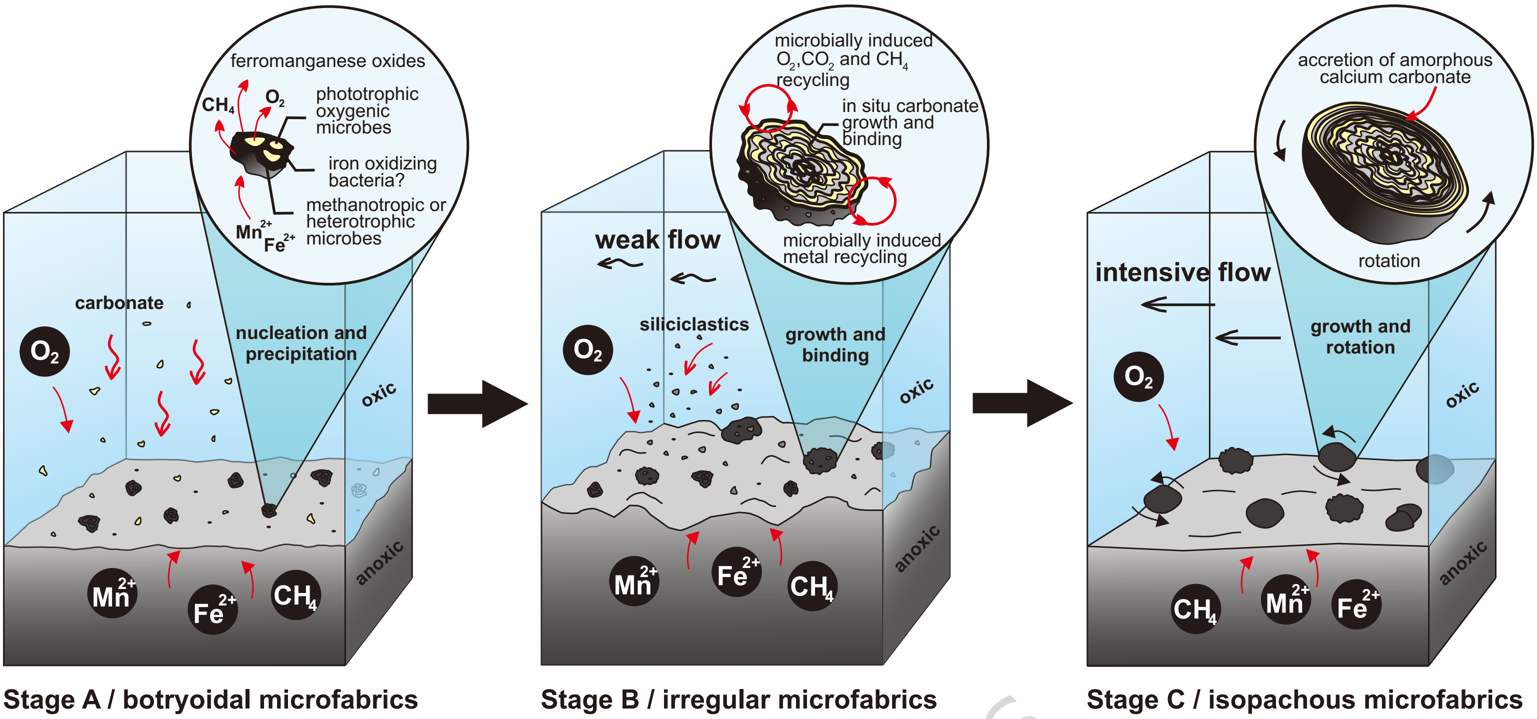
ferromanganese oxides
CH_4
O_2
phototrophic oxygenic microbes
iron oxidizing bacteria?
methanotropic or heterotrophic microbes
Mn^{2+}
Fe^{2+}
carbonate
O_2
nucleation and precipitation
oxic
anoxic
Mn^{2+}
Fe^{2+}
CH_4
Stage A / botryoidal microfabrics
microbially induced O_2,CO_2 and CH_4 recycling
in situ carbonate growth and binding
microbially induced metal recycling
weak flow
siliciclastics
O_2
growth and binding
oxic
anoxic
Mn^{2+}
Fe^{2+}
CH_4
Stage B / irregular microfabrics
accretion of amorphous calcium carbonate
rotation
intensive flow
O_2
growth and rotation
oxic
anoxic
CH_4
Mn^{2+}
Fe^{2+}
Stage C / isopachous microfabrics

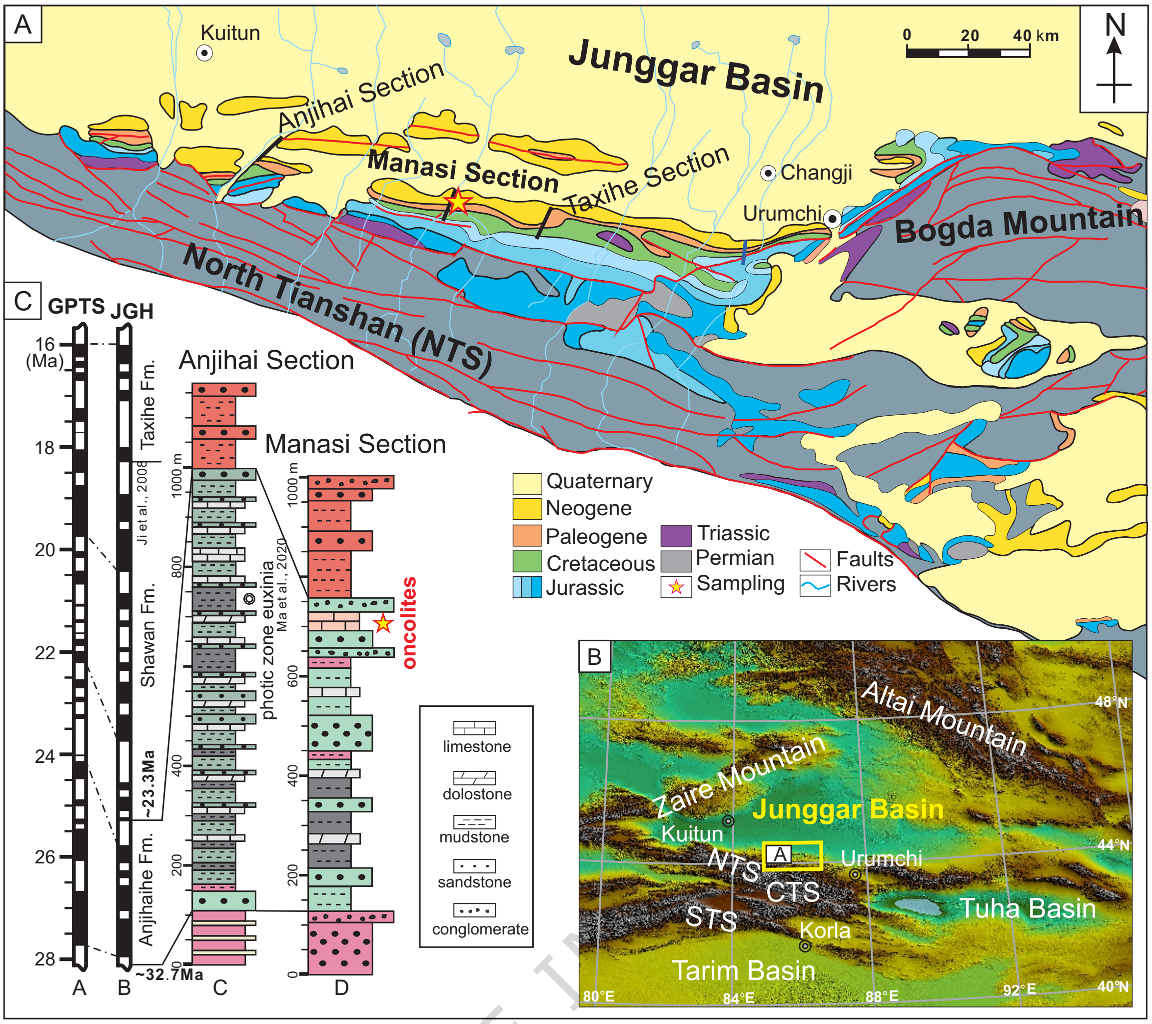
A
Kuitun
Junggar Basin
0 20 40 km
N
Anjihai Section
Manasi Section
Taxihe Section
Changji
Urumchi
Bogda Mountain
North Tianshan (NTS)
C
GPTS
JGH
16 (Ma)
18
20
22
24
26
28
Taxihe Fm.
Ji et al., 2008
Shawan Fm.
~23.3Ma
Anjihaihe Fm.
~32.7Ma
Anjihai Section
1000 m
800
400
200
0
photic zone euxinia
Ma et al., 2020
Manasi Section
oncolites
1000 m
600
400
200
0
A
B
C
D
Quaternary
Neogene
Paleogene
Cretaceous
Jurassic
Triassic
Permian
Sampling
Faults
Rivers
limestone
dolostone
mudstone
sandstone
conglomerate
B
Altai Mountain
Zaire Mountain
Junggar Basin
Kuitun
A
Urumchi
NTS
CTS
STS
Korla
Tuha Basin
Tarim Basin
48°N
44°N
40°N
80°E
84°E
88°E
92°E

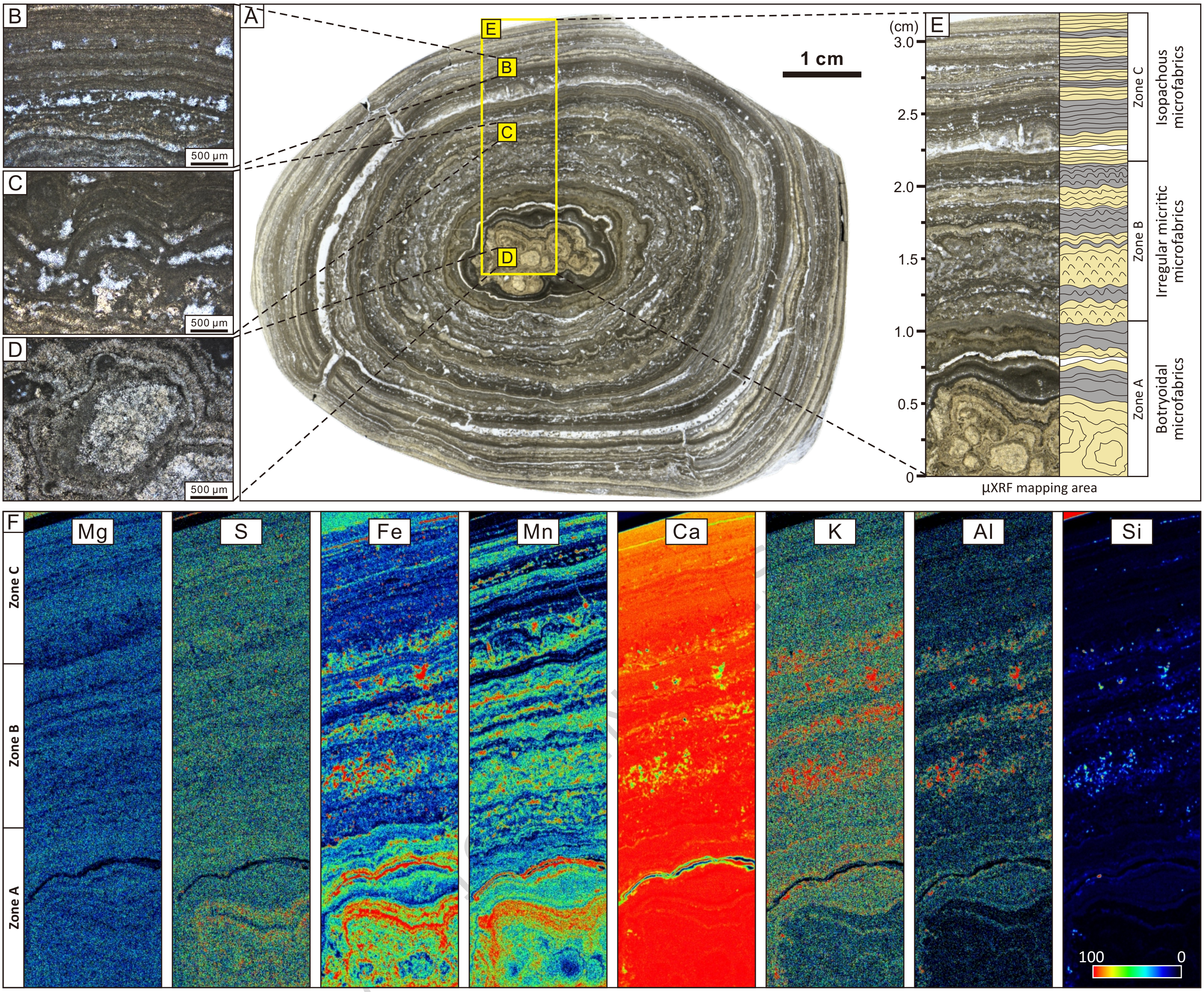
B
500 µm
C
500 µm
D
500 µm
A
E
B
C
D
1 cm
E
(cm)
3.0
2.5
2.0
1.5
1.0
0.5
0
Zone C
Isopachous microfabrics
Zone B
Irregular micritic microfabrics
Zone A
Botryoidal microfabrics
µXRF mapping area
F
Zone C
Zone B
Zone A
Mg
S
Fe
Mn
Ca
K
Al
Si
100
0

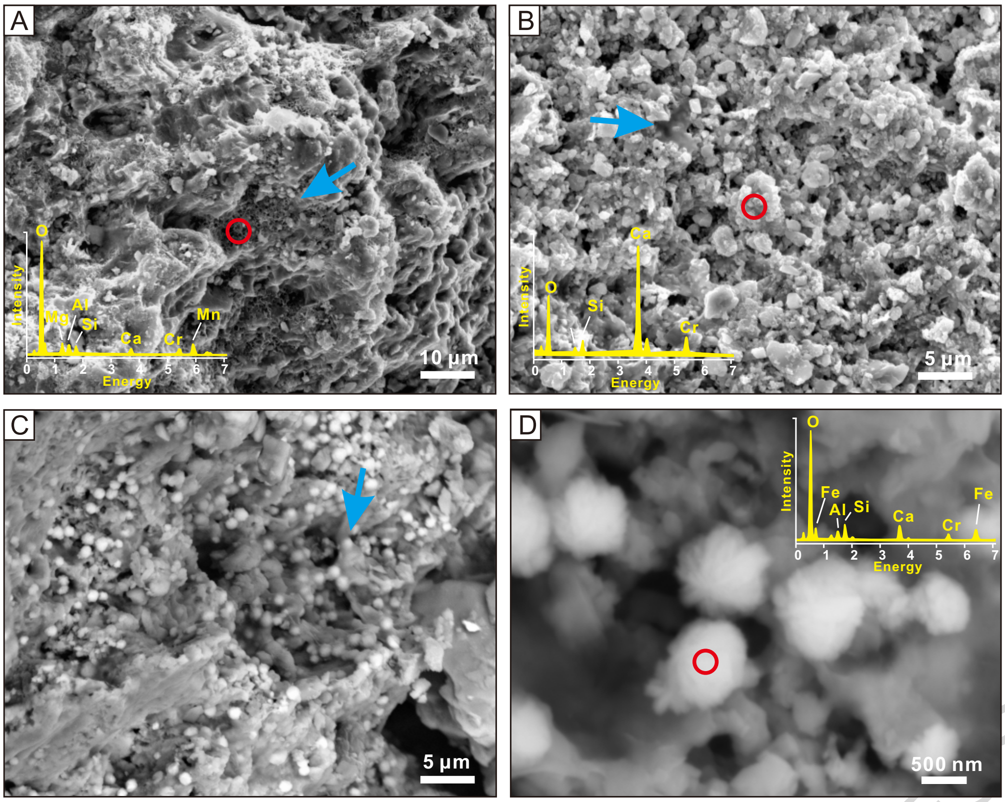
A
O
Intensity
Mg
Al
Si
Ca
Cr
Mn
0 1 2 3 4 5 6 7
Energy
10 µm
B
Ca
O
Si
Cr
Intensity
0 1 2 3 4 5 6 7
Energy
5 µm
C
5 µm
D
O
Intensity
Fe
Al
Si
Ca
Cr
Fe
0 1 2 3 4 5 6 7
Energy
500 nm

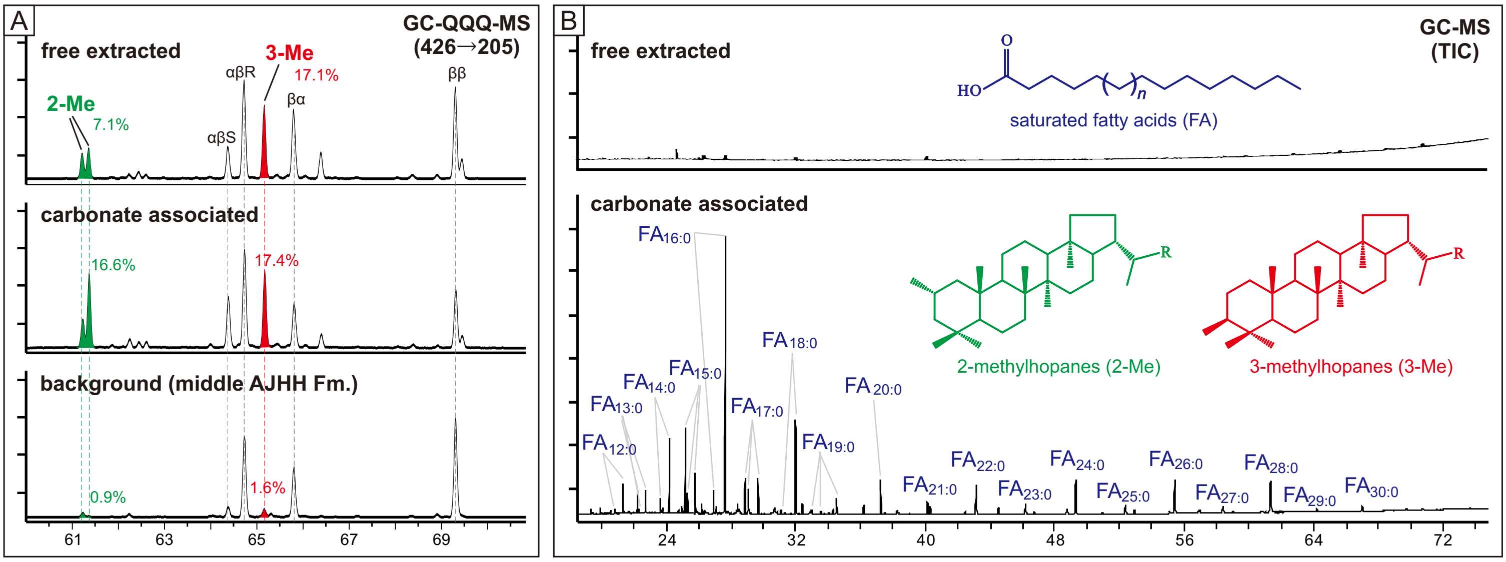
A
GC-QQQ-MS
(426→205)
free extracted
2-Me
7.1%
3-Me
17.1%
αβR
βα
αβS
ββ
carbonate associated
16.6%
17.4%
background (middle AJHH Fm.)
0.9%
1.6%
61
63
65
67
69
B
GC-MS
(TIC)
free extracted
O
HO
n
saturated fatty acids (FA)
carbonate associated
R
2-methylhopanes (2-Me)
3-methylhopanes (3-Me)
FA16:0
FA18:0
FA15:0
FA14:0
FA13:0
FA17:0
FA 20:0
FA12:0
FA19:0
FA22:0
FA24:0
FA26:0
FA28:0
FA21:0
FA23:0
FA25:0
FA27:0
FA29:0
FA30:0
24
32
40
48
56
64
72

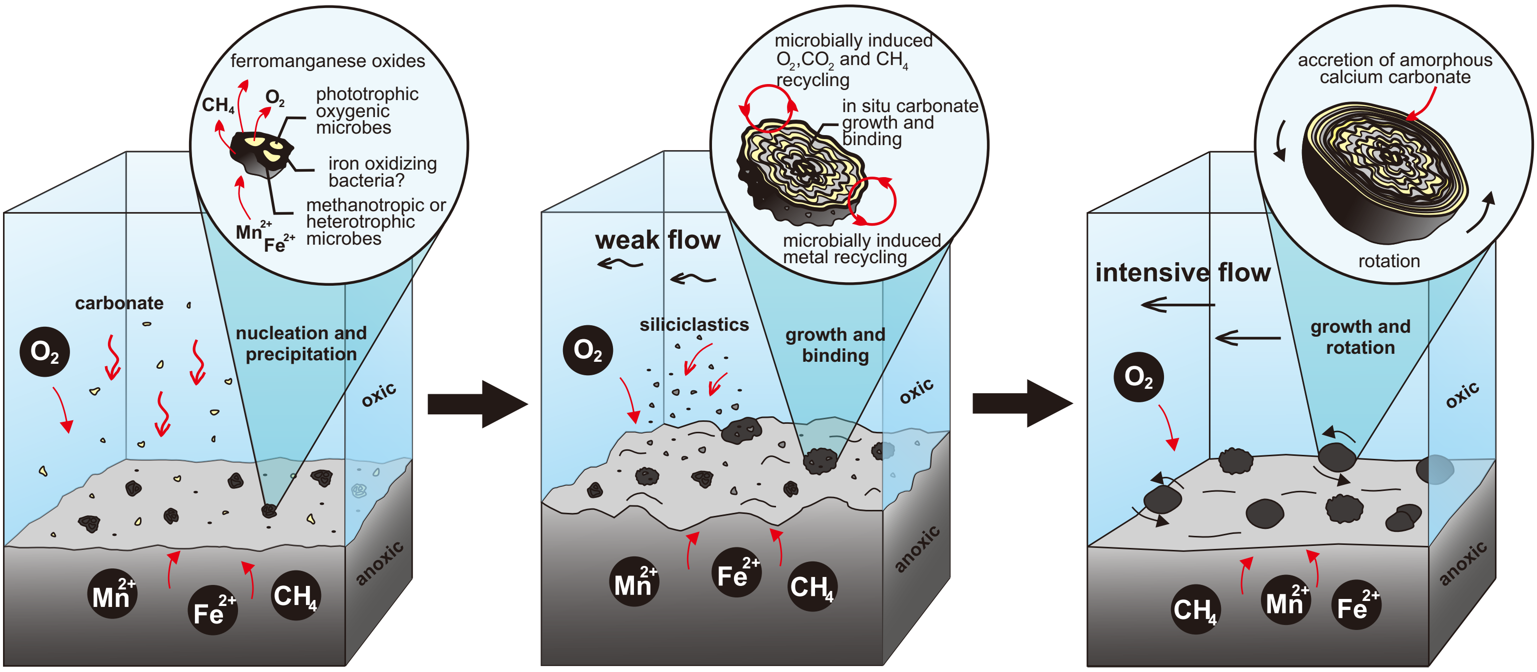

Stage A / botryoidal microfabrics

Stage B / irregular microfabrics

Stage C / isopachous microfabrics

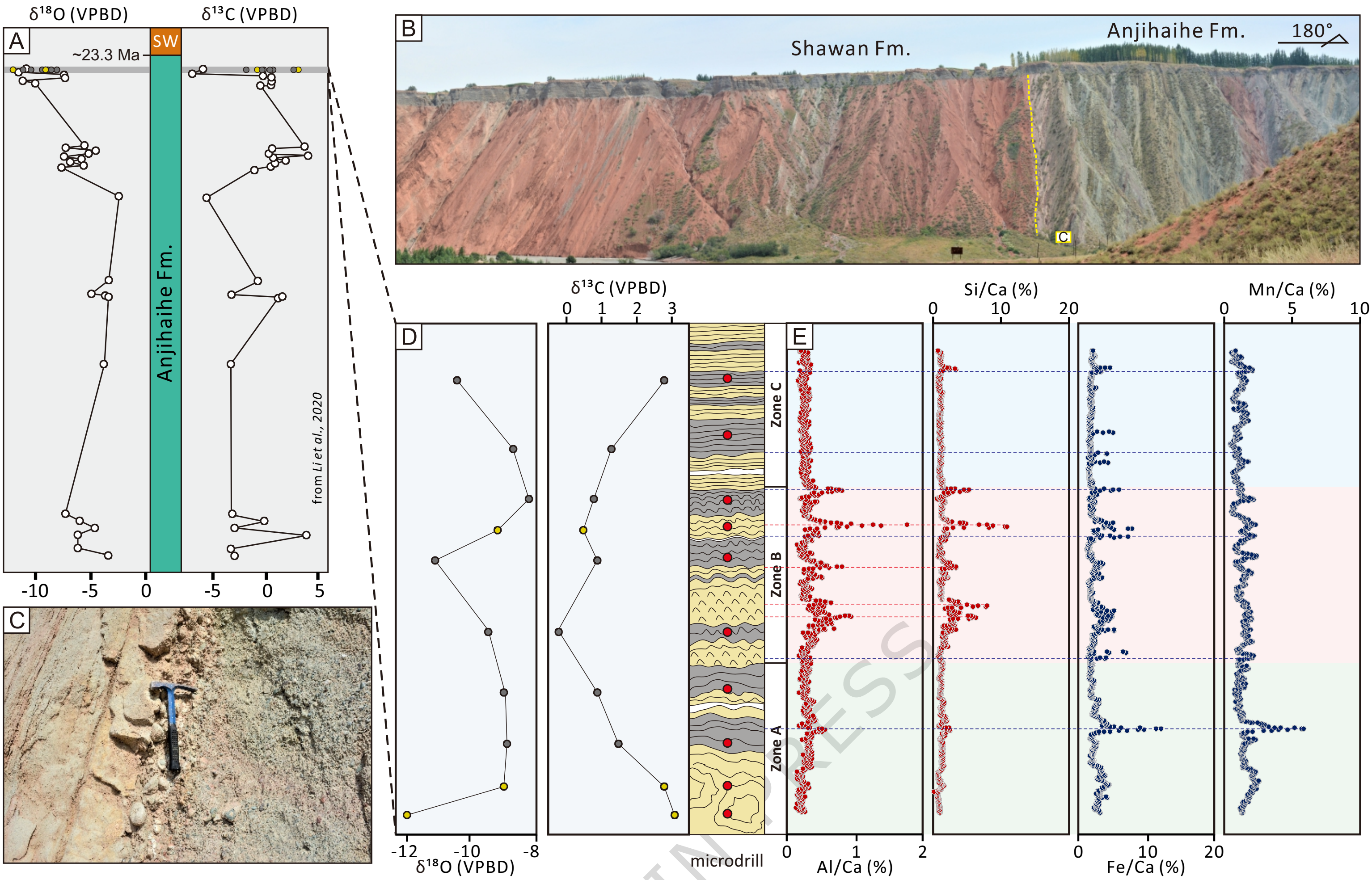
δ¹⁸O (VPBD)
δ¹³C (VPBD)
A
SW
~23.3 Ma
Anjihaihe Fm.
from Li et al., 2020
-10
-5
0
-5
0
5
B
Shawan Fm.
Anjihaihe Fm.
180°
C
C
D
δ¹³C (VPBD)
0
1
2
3
-12
-10
-8
δ¹⁸O (VPBD)
microdrill
E
Zone C
Zone B
Zone A
0
1
2
Al/Ca (%)
Si/Ca (%)
0
10
20
0
10
20
Fe/Ca (%)
Mn/Ca (%)
0
5
10